Journal of Nuclear Materials 399 (2010) 1–12

Contents lists available at ScienceDirect

Journal of Nuclear Materials

journal homepage: www.elsevier.com/locate/jnucmat

# Examination of the chemical composition of irradiated zirconium based fuel claddings at the metal/oxide interface by TEM

S. Abolhassani [a,*], G. Bart [a], A. Jakob [b]

[a] Laboratory for Materials Behaviour, Paul Scherrer Institut, 5232 Villigen-PSI, Switzerland
[b] Laboratory for Waste Management, Paul Scherrer Institut, 5232 Villigen-PSI, Switzerland

ARTICLE INFO

*Article history:*
Received 7 May 2008
Accepted 22 October 2009

ABSTRACT

Detailed post-irradiation examinations have been performed at PSI on three fuel rods with differing cladding materials revealing different corrosion behaviour. The rods had been irradiated for 3–5 cycles at Gösgen nuclear power plant (pressurised water reactor), Switzerland. As zirconium corrosion is proceeding at the metal/oxide interface, extended micro-structural analyses were performed by transmission electron microscopy (TEM), expecting to possibly reveal phenomena explaining the varying corrosion resistance. This paper reports on the distribution of oxygen at the metal/oxide interface examined by energy dispersive X-ray spectroscopy (EDS) in TEM, while other micro-structural investigations have been published earlier [1]. In order to get some statistical confidence in the analyses, three neighbouring TEM samples of each cladding variant were studied. The oxygen concentration profiles of the three alloys (i.e. low-tin Zircaloy-4, Zr2.5%Nb and extra low-tin (Sn 0.56%)) both in the oxide and metal close to the metal/oxide interface are compared. The results of the examinations show the composition of the oxide in the vicinity of the interface to be sub-stoichiometric for all three materials, indicating an oxide layer adjacent to the interface, with diffusion-controlled access of oxygen to the metal/oxide interface. The metallic parts show highest oxygen concentrations at the metal/oxide interface which are reduced towards the bulk metal, pointing towards the expected second diffusion-controlled process leading to α-Zr (O). Based on the experimental results values for the diffusion coefficients in the range of $0.8–6.0 \times 10^{-20}$ m$^2$ s$^{-1}$ are estimated for the oxygen dissolution process, the diffusion coefficient in Zircaloy-4 being six times higher than for the other two less corroding alloys. This finding is in contradiction with the present assumptions about the corrosion mechanism, and confirms the expected but not so far reported diffusion controlled oxidation of different zirconium alloys. It also points towards a corrosion rate that is at least partly governed by the diffusion coefficient of oxygen in metal that is different for different alloys, unlike what has been assumed till present.



## 1. Introduction

Zirconium and even more zirconium alloys have high resistance to oxidation despite their highly exothermal oxide formation energy which, at 300 °C, is about (−250 kcal/mol) [2]. Similar to alumina, zirconia, as refractory material, forms a very resistant oxide layer protecting the underlying substrate from further oxidation.

The oxidation reaction of Zr and its alloys takes place at the metal/oxide interface. Therefore, the oxidizing species should access the interface through the existing oxide layer in order to react with the metal and continue the oxidation process [3]. This fact should imply that the oxidation rate slows down with time, since the increasing diffusion path due to the growth of the oxide thickness causes a longer time for the oxidizing species to access the metal at the interface. However, in practice the protecting oxide layer breaks down at a certain thickness (after a so called "pre-transition phase" where the process is considered to be diffusion-controlled) and then the oxidation continues with a linear rate. Nevertheless, depending on the composition of the alloy, its heat treatment and the oxidation condition in the reactor, the rate of oxidation can change to a great extent.

The oxidation of zirconium-based claddings has been studied extensively by many different methods worldwide with the strong impetus to improve the cladding corrosion performance for extended fuel burnups [4]. The corrosion properties of the alloys developed during the last 20 years are now satisfactory both for boiling water reactors (BWR) [5] and for pressurized water reactors (PWR) [6]. The uniform corrosion can be claimed to be no more a limiting parameter for the fuel lifetime and today's alloys have also satisfactory (low) hydrogen uptake behaviour. It still happens, however, that unwanted or uncontrolled phenomena such as unfavourable

* Corresponding author. Tel.: +41 56 310 2191; fax: +41 56 310 2205.
*E-mail address:* sousan.abolhassani@psi.ch (S. Abolhassani).

0022-3115/$ - see front matter © 2009 Published by Elsevier B.V.
doi:10.1016/j.jnucmat.2009.10.060

water chemistry conditions deteriorate the corrosion resistance and lead to unexpected high general or localized corrosion.

Despite the intense and fruitful efforts spent in improving the corrosion resistance of claddings, the mechanisms responsible for improved or deteriorated corrosion resistance, are not known in detail. A debate is still going on about the existence of an innermost impervious oxide layer hindering the underlying metal from further oxidation by diffusion control. In discussing the corrosion mechanism(s) the focus lies on the cladding chemical composition, grain size, precipitates, recrystallization, texture and surface condition [7]. The fraction of oxygen dissolving in the base metal and the dissolution kinetics are assumed to vary only slightly from alloy to alloy. A rapidly corroding alloy should therefore show a shallower diffusion zone in the metal [7,8]. The same references also mention the difficulties of measuring the diffusion profiles in the metal from autoclaved samples or samples exposed to LWR operating conditions of only 300–400 °C.

The oxidation process in nuclear power reactors is not easy to examine, since long irradiation cycles have to be awaited and in-pile measurements and probe techniques (even under test reactor conditions) are nearly not existent. In addition, results of post-irradiation tests of fuel pins are not always reproducible and in some situations it is not possible to separate in an unambiguous manner material effects from hidden or obvious water chemistry changes.

Despite these difficulties, in our search for micro-structural/microchemical hints controlling or influencing the corrosion behaviour, we focus in this study, on irradiated cladding material rather than on model and/or autoclaved alloys. This approach being possible only if a Hotlab infrastructure is available, has the advantage of examining the material after exposure to a real service environment.

In a high burnup fuel characterization program performed for PWR Kernkraftwerk Gösgen - Däniken AG (KKG) in Switzerland, claddings with different alloy compositions and heat treatments were analyzed for their oxide thickness, hydrogen uptake; fuel and cladding microstructure and fission gas release. Selected cladding samples were then available for further detailed TEM microstructural investigations described already in a previous paper [1]. In this study we concentrate on the distribution of oxygen in the vicinity of the metal/oxide interface, measured on cladding samples of low-tin Zircaloy-4 (Zry-4), an extra-low-Sn alloy (ELS) and Zr2.5%Nb (Zr/Nb) by analytical TEM. The results of the oxygen concentration profiles are then discussed based on diffusion theory and compared to the respective cladding corrosion behaviour.

## 2. Materials and methods

For the present TEM work, samples were taken from three rods with alloy composition of low-tin Zircalroy-4 (1.3 wt.% Sn), of extra low tin (0.56 wt.% Sn) and of Zr2.5%Nb (2.5 wt.% Nb) showing significantly differing corrosion behaviours. Zr/Nb shows a microstructure with α-Zr and meta-stable β-Zr. Zry-4 and extra low tin (ELS) reveal an α-Zr phase, with submicron sized laves phase particles. Characteristics of each material such as the oxygen content of the alloy before irradiation and mean secondary phase particle (SPP) size, the principal irradiation and post-irradiation data of the fuel rods (estimated fluence, irradiation cycles, hydrogen pick-up fraction and circumferentially averaged peak oxide thickness values) are described in Table 1.

The table also shows the axial elevation where the TEM samples were selected from and the respective local sample oxide thickness values. In order to better compare the different alloys, the oxidation rate of each alloy is shown in a schematic graph (Fig. 1), assuming (and generalizing) linear oxidation rates for the full exposure/irradiation time. This assumption is acceptable for these materials, since the pre-transition period of about 100 days plays a minor role compared to the actual long oxidation/irradiation times of 990–1650 days, to which the claddings were exposed. The indicated final corrosion thickness values were taken from destructive examinations using scanning electron microscopy, prior to TEM sample preparations. As can be observed from Table 1 and Fig. 1, the variation of the corrosion rates of the analyzed alloys is significant; the Zr–2.5%Nb has the slowest rate and low-tin Zircaloy-4 shows 2.76 times higher rate of oxidation.

In order to prepare samples for TEM analysis, a 3 mm long ring segment of the fuel rod was used, the cladding segment was defueled and the ring was further cut in the direction parallel to the tube axis (Fig. 2) into 2 mm wide segments. The small segments of the ring were subsequently taken out of the hot cell and further decontaminated from any trace of the fuel in a shielded fume hood. Two such segments, defined by the cladding radial-axial plane were subsequently prepared side by side; their waterside oxide layer being joined together thus protected against mechanical damage during subsequent processing (Fig. 2). These samples were mechanically ground and polished to obtain specimens with ~200 μm thickness for further preparation. The thickness of TEM samples must be as homogeneous as possible for chemical analysis and lie in the range of 60–100 nm. From various methods tested, only focused ion beam milling (FIB) produced samples revealing the flatness and thickness homogeneity on both sides of the metal/oxide interface needed for TEM–EDS analysis. The FIB instrument used was an "FEI Strata DB 235 dual beam®" (DB) workstation. This instrument has an electron column with a field emission gun and is equipped with secondary electron- and a through lens detector. The ion used for sputtering was Ga. Further details of sample preparation are provided elsewhere [1,9].

The TEM study of the material was performed on a JEOL 2010 machine with an acceleration voltage of 200 keV, equipped with an Oxford Instrument energy dispersive X-ray spectrometer (EDS), using INCA software. The energy resolution of this detector is 132 eV. Pure zirconium oxide with monoclinic crystal structure from Merck was used as a standard for chemical analysis. All oxygen concentration values were converted into at.% values unless otherwise indicated.

As conditioning of the detector will influence the low energy signals of the 0.5249 keV K-α edge of oxygen, regular conditioning

**Table 1**
Irradiated fuel cladding materials studied to analyse the microstructure and composition of the waterside metal–oxide interface by TEM. The oxide thickness of the cladding at the elevation studied is given under TEM sample oxide thickness; the oxide thickness at this elevation has been measured by SEM prior to sample selection.

| Material | Sample nomination | Metal oxygen concentration (wt.%/at.%) | No. of cycles | Burnup (MWd/kg U) | Fluence estimated (n/cm$^2$) $E > 0.821$ Me V | Sample elevation from the bottom (mm) | Rod max. oxide thickness (μm) | TEM sample oxide thickness (μm) | Hydrogen Pick up (ppm) | Spp mean size (nm) |
|---|---|---|---|---|---|---|---|---|---|---|
| Extra low-tin ELS0.56 | ELS | 0.12/0.68 | 5(4.7) | 65.6 | $1.20E+22$ | 1567 | 52 | 16 | 200 | |
| Low-tin Zircaloy-4 | Zry-4 | 0.17/0.96 | 4 | 51.1 | $1.03E+22$ | 1468 | 59 | 25 | 367–460 | 190 |
| Zr–2.5%Nb | Zr/Nb | 0.12/0.68 | 3 | 41.4 | $8.30E+21$ | 869 | 16 | 6.9 | 70 | n.a.* |

* n.a.: not available.

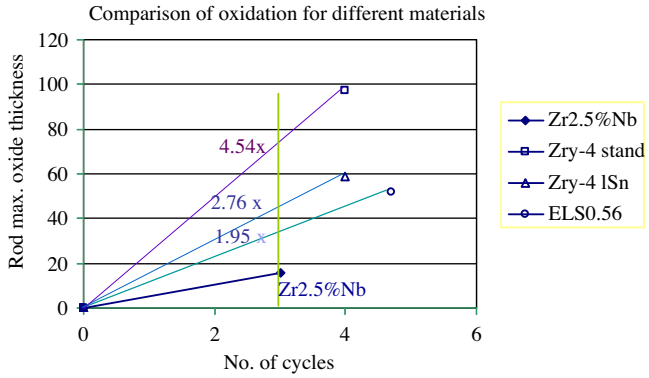


**Fig. 1.** Comparison of the oxidation behaviour of different pathfinder cladding alloys in the nuclear power plant KKG. The rod maximum oxide thickness (μm) is shown as a function of reactor irradiation cycles (~years). The indicated ratios correspond to the corrosion rate increase compared to the slowest oxidation rate of Zr2.5%Nb.

of the detector was performed. Several examinations proved that the standardless method of the INCA software was the most adapted to the calculations of the software. Prior to each measurement a test with the $ZrO_2$ reference powder was performed in order to check the validity of the oxygen counts and calculations. Despite several precautions taken it was realized that some parameters can induce artifacts in the measurements and in the results. These artifacts can have several origins:

a. The metal side of the interface can be excessively oxidized due to FIB sample preparation. FIB process can induce amorphous regions in the metal. Such amorphised metal oxidizes much faster than the bulk metal. The oxidation of zirconium and its alloys at room temperature is known to create an oxide film of only 2–4 nm thick. If the metal is amorphised to a certain depth, the oxide thickness is significantly increased and, under rare conditions, extremely high oxygen signals in areas of the "metal phase" (sometimes in the range of 50%) could be detected. However, since the diffraction pattern of the metal qualitatively indicates the degree to which oxidation has taken place, such regions were not considered for oxygen concentration quantification, and the measurements were rejected.
b. The thickness variation even of the FIB prepared TEM samples, is significant; therefore it is not possible to assume a homogeneous thickness throughout the TEM sample. Special care was therefore taken to select uniformly thick sample regions and there were again samples which had to be rejected due to large thickness variations.
c. The standard FIB instruments use a Ga ion beam. The FIB sample preparation can therefore lead to Ga implantation at the surface. In such cases the structure and composition of the surface will change. Therefore, if the Ga concentration was measured to be above 0.5–1 at.%, another region was selected for analysis.
d. Above a given sample thickness, the oxygen signal will be absorbed by zirconium. Therefore the thickness of the samples had to be estimated for thickness corrections and normalization. Electron energy loss spectroscopy was used to measure the thickness of the samples.

The measured data points were carefully judged to be included or rejected due to such artifacts. As there is a risk to over interpret single extremely localized TEM analytical findings, the oxygen profiles were measured for each cladding type on three neighbouring samples. The repetition helped improve the statistics of the measured results and to get some implicit information about possible sample preparation artifacts. Overall we assume our results to show accuracy in the range of ±2–10% depending on the oxygen concentration.

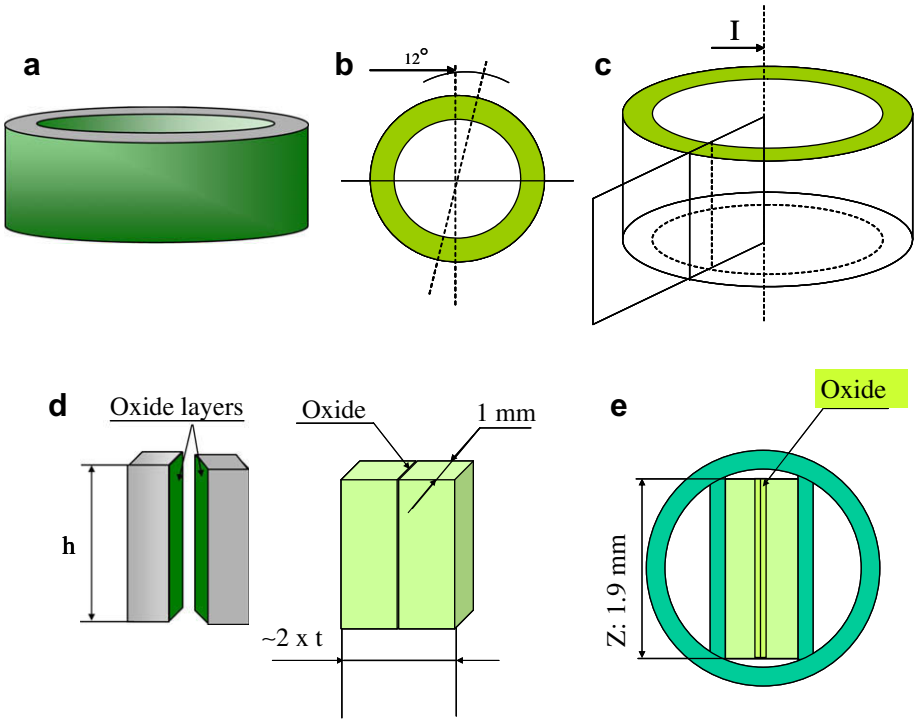


**Fig. 2.** (a–e) Schematic diagram of the sample preparation steps prior to focused ion beam milling [9]. From (a–c) steps are shown for the cutting of the segments of the oxidized tube. (d) Two segments are glued together with the oxide layers facing each other. (e) The joint piece was resized to fit into the Ti holder and the surface of the sample was finely polished.

## 3. Experimental results

The oxygen concentrations were measured across the metal/oxide interface into the adjacent oxide and metal phases at steps of ~50–200 nm. The analysis was extended to a distance of 2000–4000 nm on the two sides of the interface, depending on the quality of the FIB sample. The concentration profiles in at.% values are shown in Figs. 3–5 together with the TEM bright field view of the metal/oxide interface of one of the samples for each material. The TEM images reveal very clearly the metal/oxide interface and a series of cracks in the oxide region parallel to the metal/oxide interface. The morphology and crystal structure of the two sides of the interface, and the different phases present in the oxide are described elsewhere [1]. The oxygen concentrations in the range of 40% related to a structure of ω-Zr have been reported by previous studies [10]. The phases present in the oxide in Zr2.5%Nb alloys have been studied by previous authors [11–13]. The stability of these phases can be due to their atomic composition and also due to the stresses built-up around the two sides of the interface.

The oxygen profiles reveal the following general trends:

- All three materials show a drop of oxygen concentrations in the oxide near the interface.
- All materials reveal oxygen concentrations in the metal side, diminishing with distance from the interface.

In detail the three alloys exhibit the following trends in oxygen concentrations:

*Low-tin Zircaloy-4*: The three analyzed samples examined of this alloy showed a stoichiometric oxide up to a distance of only 150–200 nm from the metal/oxide interface (Fig. 3). The oxygen concentration shows little scatter between the three samples and lies in the range of 65–70 at.%. Only the nearest points to the interface reveal a slight substoichiometry of a few at.%. The presented TEM view for this sample also shows the closest proximity of tangential cracks to the metal/oxide interface. The oxygen concentration in the metal close to the interface is quite high and shows values between 20 and 40 at.%, with a significant spread between the three characterized samples. The concentrations drop to lower values at a distance of 500–1000 nm but stay relatively high (12–22 at.%) on all samples over the regions analyzed from the interface, again with large scatter in the results from the individual samples. The high oxygen values in the metal side away from the interface can be explained by an air-formed 2–5 nm thick oxide layer, which will form on both surfaces of the 70–100 nm thick TEM samples and amounts to a relative oxygen contamination of 5–17%. Close to

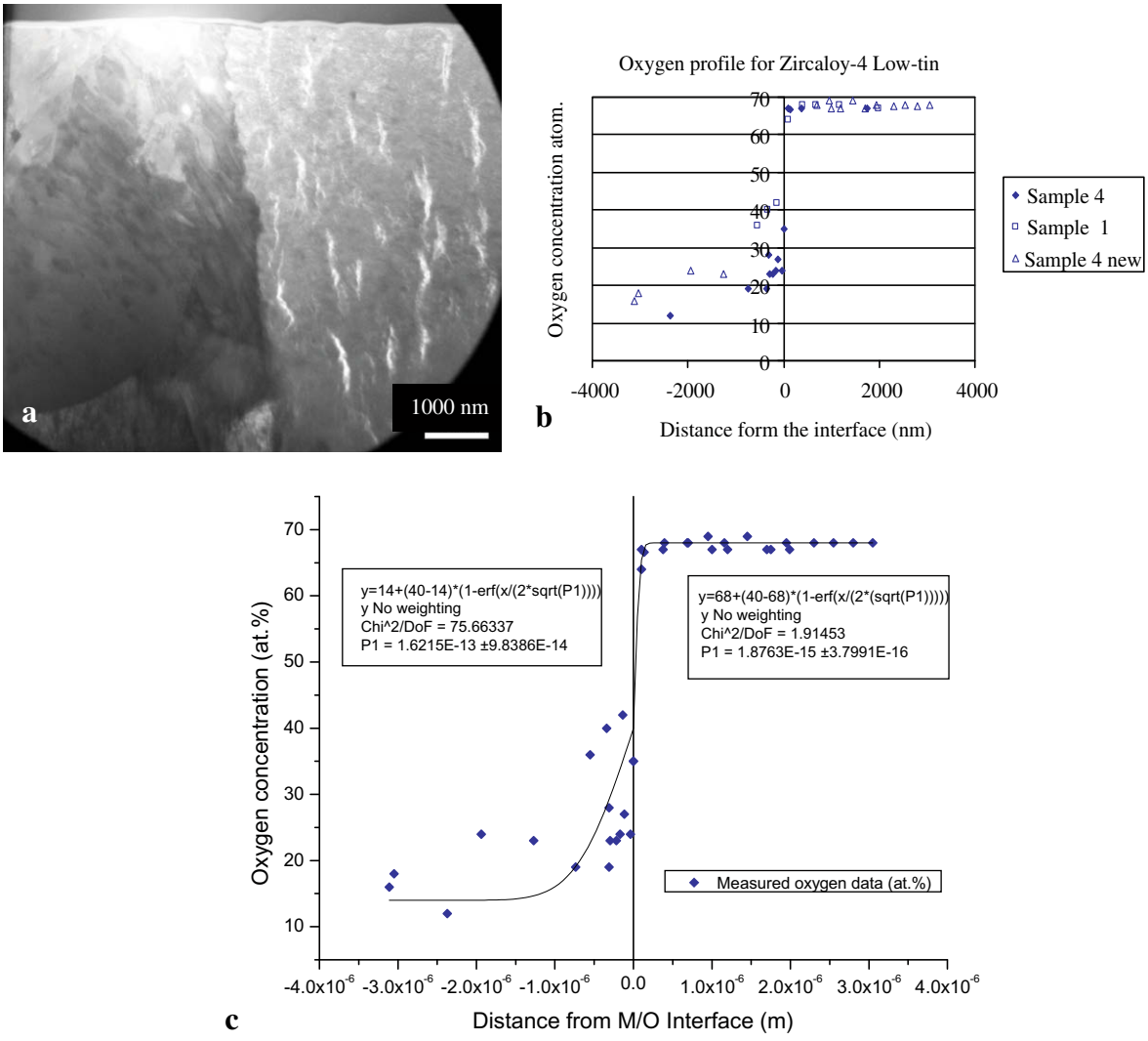


**Fig. 3.** Oxygen concentration profiles of the metal–oxide interface of low-tin Zircaloy-4. (a) TEM bright field contrast of one FIB sample; (b) oxygen profiles at the metal–oxide interface for three different FIB lamellae; (c) calculated best fits for the experimental profiles; it is to note that in these data $P_1$ represents the product of $D*t$ and does not represent the diffusion coefficients.

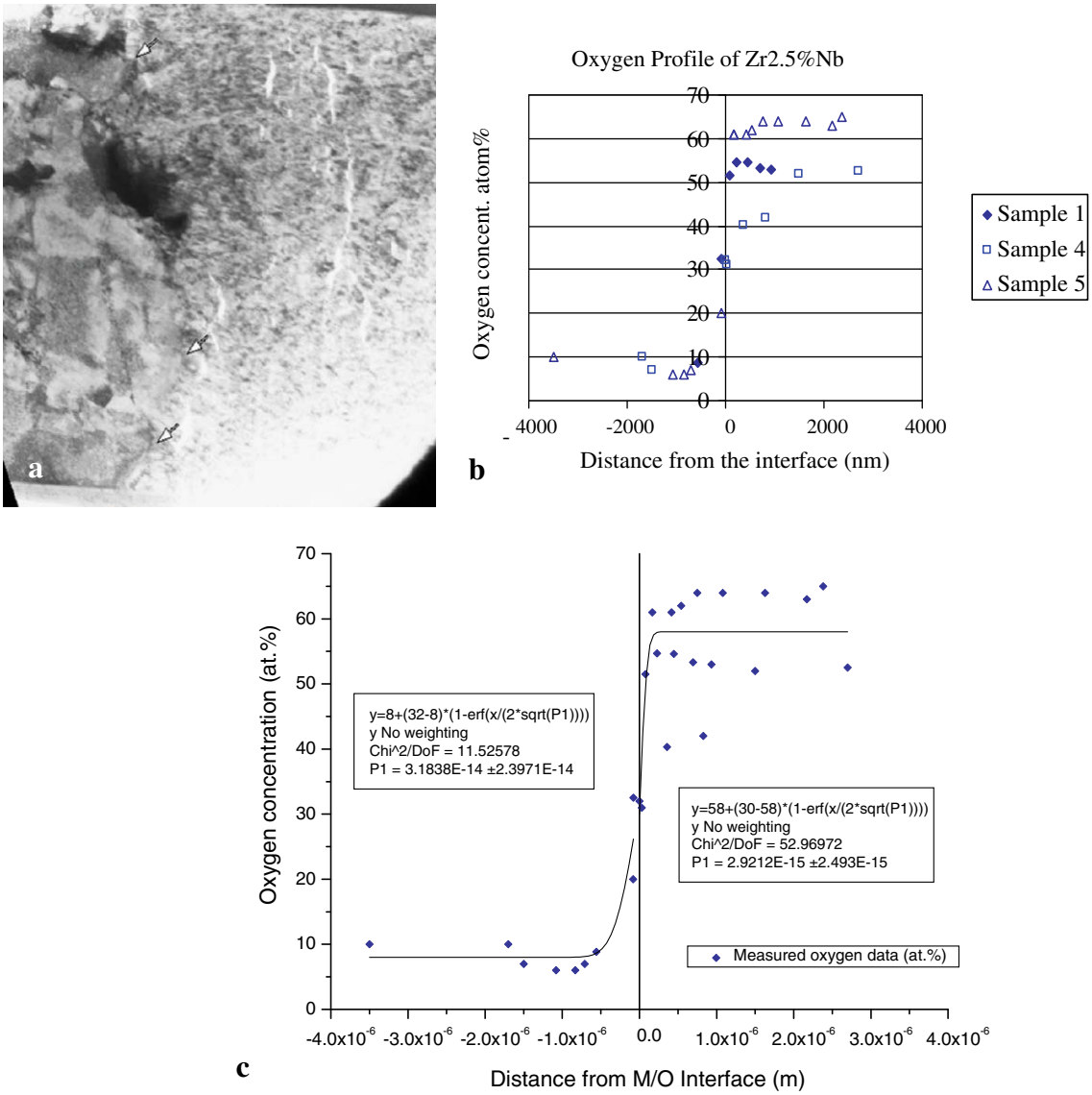


**Fig. 4.** Oxygen concentration of the metal–oxide interface of Zr–2.5%Nb. (a) TEM bright field contrast of one FIB sample; (b) oxygen profiles at the metal–oxide interface for three different FIB lamellae; (c) calculated best fits for the experimental profiles; it is to note that in these data $P_1$ represents the product of $D*t$ and does not represent the diffusion coefficients.

the interface, however, with true oxygen concentrations of ~30 at.%, the oxygen contamination due to the air-formed films is only in the range of 3 at.%. The values of up to 40 at.% which are above the solubility limits are usually related to different phases, as mentioned before the ω-Zr has been mentioned, the other possibility can be that as the high values both in the oxide and the metal phase are from one single sample, there might have been an error in measurement for this single sample. Nevertheless the principal information of the oxygen profiles at both sides of the metal/oxide interface, with a slight concentration drop from stoichiometric oxide only close to the oxide interface and a rather high oxygen concentration in the adjacent metal is real and significant.

*Zr–2.5%Nb*: The oxygen concentration of the Zr/Nb samples are presented in Fig. 4. The analyzed concentrations in the oxide reveal a rather large scatter from sample to sample but in principle show a significant substoichiometry of 40–60 at.%; up to a distance of 3000 nm from the metal/oxide interface; being the farthest positions reachable in our samples. The equilibrium phases for the Zr–2.5%Nb are α-Zr with Nb concentrations of ⩽0.6 wt.%, and β-Nb with Nb concentrations of ⩾85 wt.%. The equilibrium state however is not reached during the alloy fabrication and meta-stable phases are retained from the high temperature state [13–15]. A supersaturated α-Zr also called α′ is formed by martensitic transformation and a β-Zr phase is retained with varying Nb concentrations ranging from 15 to 20 wt.%. This phase could subsequently transform into β-Nb during long annealing times in the temperature range between 525 and 570 °C [14]. The cladding variant examined in this study revealed an α-Zr matrix containing ⩽0.6 at.% Nb, a supersaturated α-Zr (α′ phase) with varying Nb concentration of ⩽5–6 at.% Nb, and a β-Zr phase with an Nb concentration ranging between 14 and 24 at.% present at the grain boundaries of the α-Zr matrix. To estimate the inhomogeneity of the oxide, elemental point analyses were performed for this cladding in one sample parallel to the interface at a distance of about 1500 nm away from the latter (Fig. 6). Again they show a general trend of slight oxygen substoichiometry and the varying composition of Nb in the

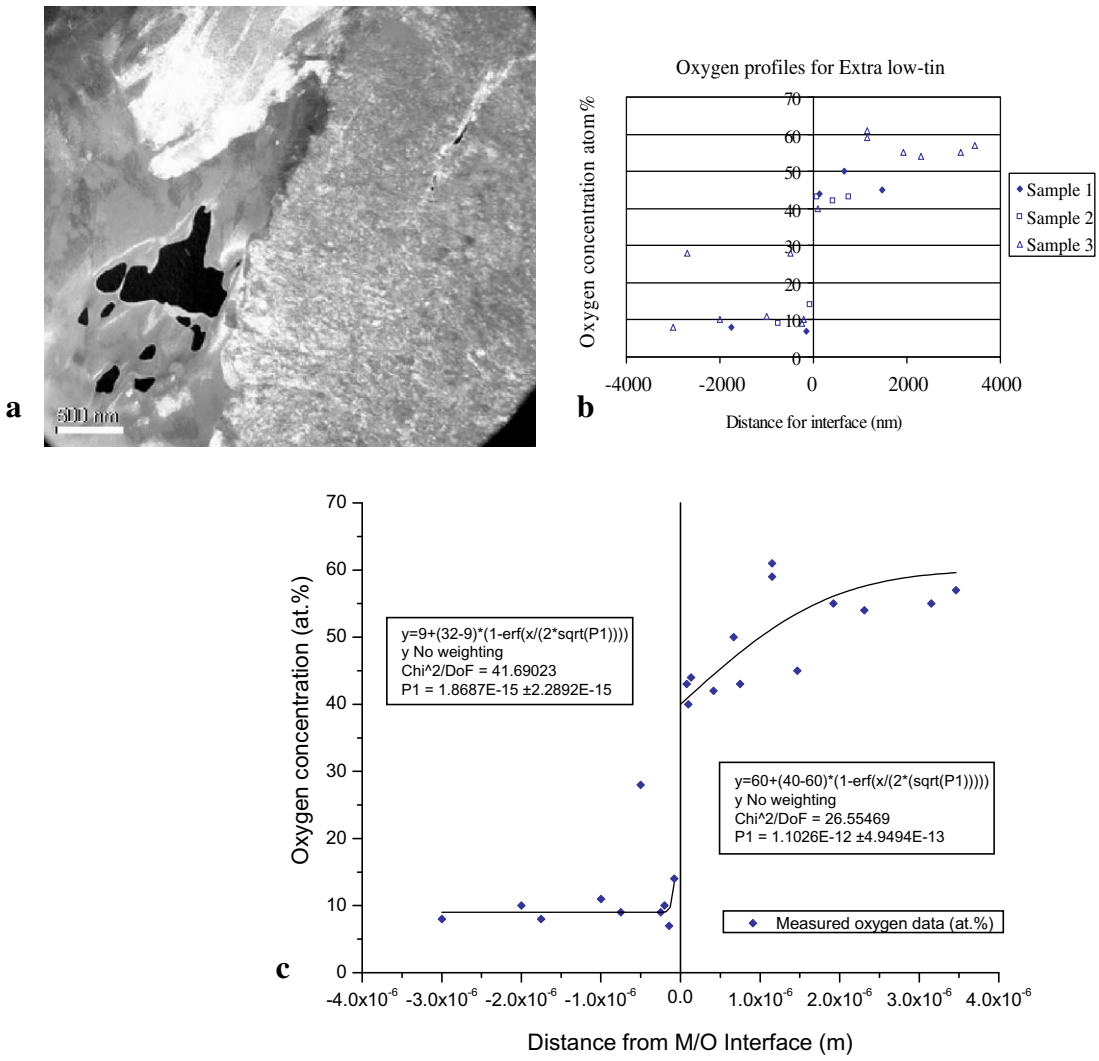


**Fig. 5.** Oxygen concentration of the metal–oxide interface of extra low tin ELSn 0.56. (a) TEM dark field contrast of one FIB sample. The dark region in the metal side of the interface is a hole created during FIB sample preparation; (b) oxygen profiles at the metal–oxide interface for three different FIB lamellae, in the regions where the samples have remained intact; (c) calculated best fits for the experimental profiles; it is to note that in these data $P_1$ represents the product of $D*t$ and does not represent the diffusion coefficients.

metal phase is observed to the same extent in the oxide. In order to exclude oxygen concentrations of β-Zr in the oxygen profiles of Fig. 4, oxygen point analyses with Nb concentrations >5 at.% were excluded.

The microstructure of the TEM image in Fig. 4 reveals a less expressed, and not very distinct transition at the metal/oxide interface compared to the Zry-4 and ELS samples and fewer, and more distant tangential cracks from the metal/oxide interface. It was repeatedly argued that such a cracking pattern could be an artefact due to sample preparation. But a recent study performed by three-dimensional reconstruction of images obtained by the "slice and view" option of FIB, has proved that the cracks in the oxide layer parallel to the metal/oxide interface are extending in two dimensions over >10 μm and therefore cannot be an artefact of FIB-milling (Fig. 7).

The metal side of the interface shows significantly lower oxygen concentrations than that observed in the low-tin Zry-4. Values of 20–30 at.% are detected only within 100–200 nm from the interface. Here the oxygen concentrations at distances greater than 500 nm drop to values of 6–10 at.%; values significantly lower than in the Zircaloy-4 case, revealing also less scatter among the individual samples. The oxygen concentrations in the bulk metal can be explained by the oxide films formed at the ambient atmosphere after TEM sample preparations.

*Extra low tin (0.56 wt.% Sn)*: The oxygen concentration profiles are presented in Fig. 5. Again the oxide close to the interface shows significant substoichiometry with oxygen values of only 40–60 at.% up to a distance of 3000 nm. Variations from sample to sample are significant but the general trend of expressed substoichiometry is evident. As in the case of Zr/Nb, the TEM image of the presented ELS sample shows fewer and more distant tangential cracks from the metal/oxide interface. The interface is again clearly marked as in the case of Zircaloy-4. The TEM image also shows areas with missing metal phase and as such, gives hints about the difficulties encountered in sample preparation. Such holes occur when samples are bent during the last stages of the FIB milling process due to stresses between the oxide and the metal [9]. The oxygen concentration in the metal phase close to the metal/oxide interface is limited to 10–15 at.% and drops within ~200 nm to a value of 6–10 at.% without further reduction in value while increasing distance from the interface. As in the Zr/Nb case, the oxygen concentrations in the

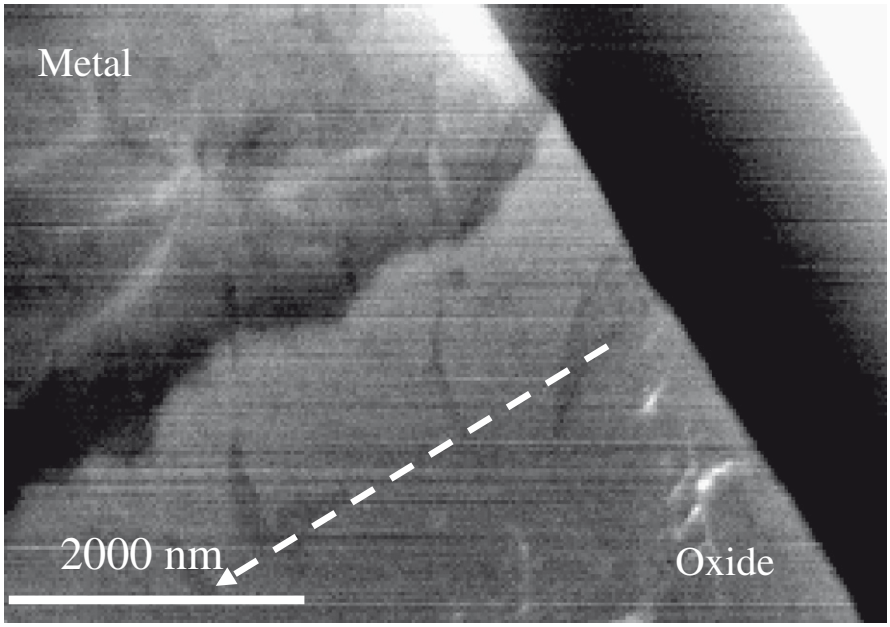


| Data | O | Ga | Zr | Nb |
|---|---|---|---|---|
| Position (1) | 63.75 | | 34.71 | 1.53 |
| Position (2) | 61.43 | 0.26 | 36.35 | 1.96 |
| Position (3) | 62.29 | | 35.70 | 2.01 |
| Position (4) | 61.87 | | 35.26 | 2.87 |
| Position (5) | 60.45 | | 33.84 | 5.71 |
| Position (6) | 60.67 | | 36.48 | 2.85 |
| Position (7) | 62.95 | | 37.05 | |
| Position (8) | 62.72 | | 35.69 | 1.59 |
| Position (9) | 62.05 | 0.23 | 37.72 | |
| Position (10) | 61.72 | 0.23 | 36.65 | 1.39 |
| Point analysis oxide interface | 61.55 | 0.23 | 36.53 | 1.68 |
| Point analysis oxide interface no. 2 | 62.34 | 0.16 | 36.11 | 1.28 |
| Max. | 63.75 | 0.26 | 37.72 | 5.71 |
| Min. | 60.45 | 0.16 | 33.84 | 1.28 |

**Fig. 6.** Results of STEM-EDS point analysis on Zr2.5%Nb sample no. 3, showing the variation of the oxygen signal in the oxide. All values are in at.%. The arrow indicates the direction of measurements presented in the table.

metal show less scatter and generally lower values than for Zircaloy-4.

## 4. Discussion and diffusion calculations

In our search for valid explanation to elucidate the different corrosion behaviour of the claddings, when approaching high burnup under normal LWR operation, we focused on engineered material from pathfinder fuel pins of different cladding materials, irradiated to intermediate burnup levels. The FIB-based sample preparation and applied TEM elemental analysis is quite elaborate and includes several uncertainties (such as the final sample thickness, amorphization and oxidation during sample preparation) which we have taken into account and which lead to estimated uncertainties in our results of ±10%. Nevertheless, the results of all samples indicate (for low-tin Zircaloy-4) a smaller, or (in case of ELS and ZrNb cladding) a more expressed oxygen depletion in the oxide layer close to the metal interface.

We interpret this depletion which we detected at the micrometer scale, as oxygen diffusion profile. Thus our results clearly support the concept of an innermost, impervious barrier layer hindering direct access of oxygen for further oxidation. In the case of Zry-4 this barrier layer is significantly thinner than in the two other materials and is limited to 100–200 nm. Our oxygen profiles are an instant view of the ongoing corrosion process. The oxidation process led to a porous outer oxide layer in the range of a few micrometers (for the Zr/Nb samples) and up to more than 20 μm (for the Zry-4 samples), and overall, in zero order approach, showed approximately linear corrosion kinetics. We assume, however, the corrosion process to consist of a succession of cyclic and local diffusion-controlled steps with intermittent breakdown of the stressed layers. Such cyclic diffusion-controlled corrosion steps have been described by several authors [16–18]. In this study we do not examine this cyclic behaviour, but focus on the very last diffusion layer at the interface. The local oxygen diffusion process within this impervious oxide layer is interrelated to the oxygen diffusion process into the metal phase,

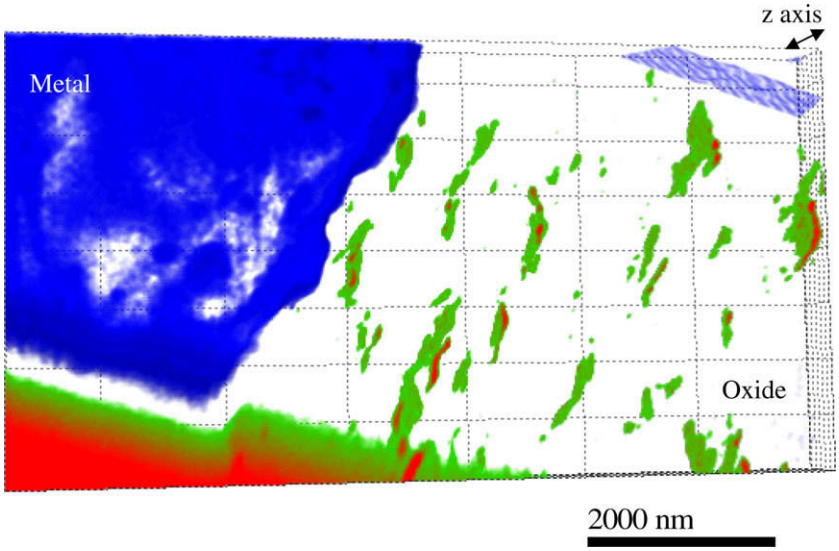


**Fig. 7.** Three dimensional reconstructions of images after repeated slice-cutting by FIB into the interface of a Zr/Nb cladding sample. Cracks in the oxide layer parallel to the M/O-interface are extending in two dimensions over >10 μm. It is therefore concluded that these cracks are not FIB cutting artifacts.

leading to α-Zr (O). The values for the diffusion coefficients in the metal phase for $T = 619$ K (corresponding approximately to the temperature of the KKG fuel rods at the sample elevation and at metal/oxide interface position) are estimated to lie around $10^{-19}$–$10^{-21}$ $m^2\ s^{-1}$ [19,20], the corresponding diffusion coefficients in the oxide layer are about $10^4$ times larger [21]. The mathematical handling of the kinetics of such a combined two-phase diffusion process with moving boundaries is well described [22–26], but this mathematical treatment cannot be applied for the present results as there is no time sequence of diffusion profiles available in the oxide. Even more it is impossible to take into account any charge transfer resistance at the interface as discussed e.g. by Nanikawa and Etoh [23] and Eloff et al. [27]. Such a space charge alters the oxygen or oxygen-vacancy diffusion in the pre-transition oxidation kinetics.

### 4.1. Modelling of the oxygen profiles

Two steps were considered for the modelling in the present study.

At a first step, the metal and the oxide were treated separately to find the best fit for the experimental curves. Based on the discussion above it was assumed that in the oxide, only very near the metal–oxide interface bulk diffusion is the prominent transport process for oxygen, and for the oxide away from the interface the bulk diffusion is not the prominent transport mechanism and the oxide layer is not modelled. The absence of micro fractures and fissures closest to the metal/oxide interface justifies this assumption. Furthermore it was supposed that diffusion in the metal and in the oxide phase happens both homogenously and isotropically and, hence, the migration of oxygen is well described by a one-dimensional diffusion model. For simplicity reason, it was further postulated that the diffusion coefficient is constant in space and time and independent of the local oxygen concentration. Values for the boundary conditions were assumed to be constant and diffusion of oxygen happened in a semi-infinite medium where the effects of the second boundary are negligible. In both domains – the metal and the oxide phase – a non-zero initial condition for oxygen was presumed. Based on these assumptions the solution of the transport process describing the oxygen concentration profiles in the metal and oxide phase, can be expressed as follows [24]:

$$C(x,t) = (C_1 - C_0)\mathrm{erfc}\left(\frac{x}{2\sqrt{Dt}}\right) + C_0; \quad x \in [0,+\infty],\ t \geqslant 0. \tag{1}$$

$C(x, t)$ (at.%) represents the oxygen concentration at distance $x$ (m) from the interface and time $t$ (s), $C_0$ (at.%) is the oxygen concentration at infinite distance from the interface, $C_1$ (at.%) is the oxygen concentration at the metal/oxide interface and erfc the complementary error function. $D$ ($m^2\ s^{-1}$) corresponds to the diffusion coefficient for the oxide or the metal phase. It is obvious that Eq. (1) satisfies the initial condition $C(x, t \leqslant 0) = C_0$ and the upper boundary condition $C(x = 0, t > 0) = C_1$ as well as the second boundary condition $C(x \to \infty, t > 0) = C_0$.

As mentioned before at this stage, Eq. (1) was used to calculate the best fit of the measured oxygen profiles including all, equally weighed data points of the individual samples using Origin 7's data analysing feature [28]. The outcome of the best fit diffusion curves is added to the Figs. 3–5. However, not knowing the actual times for this diffusion-controlled process, only values for the product $P_1 = D * t$ can be extracted. The curves of the three materials qualitatively indicate a longer diffusion distance within the metal phase, and higher oxygen concentration at the interface for the faster corroding Zircaloy-4 sample(s) which, at the same time show(s) stoichiometric oxide closest to the interface.

### 4.2. Diffusion coefficient in the oxide

As discussed above the experimental results show a substoichiometry in the oxide, the extent of which varies from one alloy to another. This phenomenon has been studied and confirmed recently by other methods [29,30]. The post transition oxidation in Zr alloys is not controlled by bulk diffusion of oxidizing species through oxide, but other routes such as micro-cracks are considered to be responsible for the oxygen transport. For the last few layers of oxide before the interface showing the impervious layer, the lack of information about the time factor, means that the diffusion coefficient in this layer cannot be derived.

The curvature of the oxygen profile in the oxide layer near the interface, represents a combination of oxide composition, oxygen dissolution and oxygen diffusion.

At a second stage, the calculation of diffusion coefficients only in the metal was performed.

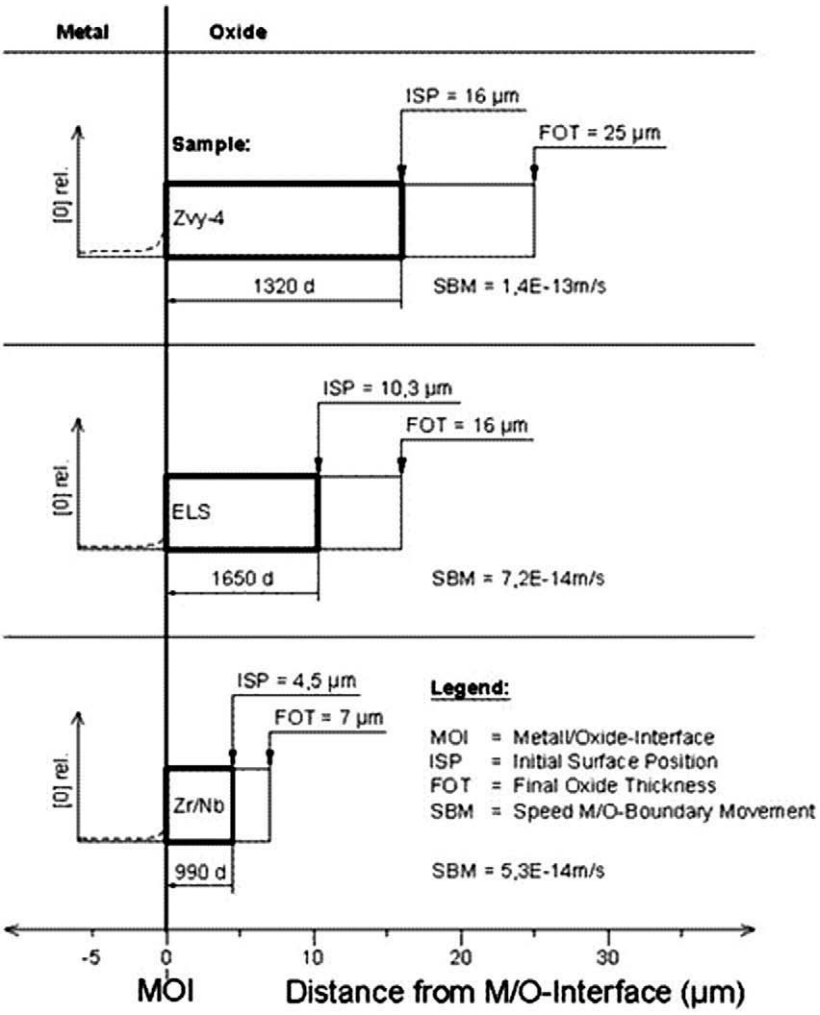


**Fig. 8.** Schematic diagram of moving M/O boundary during cladding corrosion process.

### 4.3. Diffusion calculations in the metal

While information of the actual diffusion time for the oxide diffusion part is missing due to sequential oxide break down, the actual time leading to the metallic diffusion profiles can be assumed to correspond to the full fuel irradiation time, assuming in parallel that the metal/oxide boundary due to oxidation has moved with "linear rate" towards the metal phase. This assumption is realistic, since in all oxidation analyses the rate of oxidation is reported to be linear in the post transition phase. Schematically the moving boundary process is depicted in Fig. 8. In line with the first modelling attempt a 1D diffusion model with homogeneous and isotropic transport properties was applied. However, a moving boundary representing the corrosion front linearly proceeding with time was now considered in the model. The moving metal/oxide (M/O) interface was described with the help of the arbitrary Lagrangian–Eulerian (ALE) method. Only the temporal evolution of the oxygen in the metal domain was modelled. The oxygen concentration in the oxide layer entered the model only as a boundary condition. Close to the metal–oxide interface a maximum element size of $10^{-7}$ m was chosen so that further mesh refinements did not change significantly the computational results. The initial mesh is provided in the Appendix.

**Table 2**
Input data for inverse modelling of measured oxygen profiles of three different zirconium alloy tubes and best fit data (inclusive $1\sigma$-standard deviation) for calculating the diffusion coefficient $D$ in the metal using COMSOL software. $C_1$ is the constant oxygen concentration (at.%) at the moving metal/oxide boundary.

1. Zry/low tin (diffusion profile determined after 1320 days)
   $C_1(x = 0, t > 0) = 40$ at.% (boundary condition, constant in time)
   Oxygen background concentration = 14 at.% (homogeneous, constant in time)
   Velocity of the corrosion front $v(t) = 14.03 \times 10^{-14}$ m s$^{-1}$ (constant in time)
   $D \pm \Delta D = \left(60 \pm \frac{200}{50}\right) \times 10^{-21}$ m$^2$ s$^{-1}$
2. ELS (diffusion profile determined after 1650 days)
   $C_1(x = 0, t > 0) = 40$ at.% (boundary condition, constant in time)
   Oxygen background concentration = 9 at.% (homogeneous, constant in time)
   Velocity of the corrosion front $v(t) = 7.225 \times 10^{-14}$ m s$^{-1}$ (constant in time)
   $D \pm \Delta D = \left(10 \pm \frac{40}{7}\right) \times 10^{-21}$ m$^2$ s$^{-1}$
3. Zr2.5%Nb (diffusion profile determined after 990 days)
   $C_1(x = 0, t > 0) = 40$ at.% (boundary condition, constant in time)
   Oxygen background concentration = 8 at.% (homogeneous, constant in time)
   Velocity of the corrosion front $v(t) = 5.267 \times 10^{-14}$ m s$^{-1}$ (constant in time)
   $D \pm \Delta D = \left(8 \pm \frac{8}{4}\right) \times 10^{-21}$ m$^2$ s$^{-1}$

Again constant (Dirichlet) boundary conditions as well as a non-zero initial condition for oxygen in the metal phase were assumed. The corresponding data for initial and boundary conditions and

the values for the velocity of the corrosion front for all three alloys are presented in Table 2. The partial differential equation for diffusion:

$$\frac{\partial C}{\partial t} = D\frac{\partial^2 C}{\partial x^2} \tag{2}$$

was numerically solved with the help of COMSOL/Multiphysics, a proprietary software package based on the finite element method and using high-performance solvers [31]. The measured oxygen data in the metal were used as the basis for the regression procedure with $D$ ($m^2\ s^{-1}$) the diffusion coefficient as the most important regression parameter.

It has to be mentioned that values for the initial as well as for the boundary condition at the metal/oxide interface are burdened by uncertainties and are – in principle – free for adjustment, too. However, it turned out that varying the background oxygen concentration and the value for the oxygen concentration at the metal/oxide interface was much less sensitive than changed values for $D$. This observation can be well demonstrated by the example provided in Fig. 9 on the ELS material. The fitting was done by repetitive forward modelling and by a visual estimation of the goodness of the fit along with a careful scrutiny of its underlying parameter values. For the estimation of the uncertainty of the best fit, the value for $D$ was varied systematically until calculated oxygen profiles in the metal were enveloping most of the measurements. The range in $D$ was then declared as the $1\sigma$ standard deviation error of the best-fit parameter. Due to the prominent scattering of the measured data, large uncertainties for $D$ had to be accepted, however for all three alloys the best-fit parameter values lie in the expected range of $10^{-20}\ m^2\ s^{-1}$ [16,17,19]. The diffusion coefficient for the Zry-4 case is about six times higher than the values for the ELS and Zr/Nb samples, the diffusion coefficient for Zr/Nb being slightly lower than for ELS.

In order to better understand the advantage of using a moving boundary for the COMSOL calculation, the comparison of an analytical solution and a moving boundary solution of the diffusion coefficient of oxygen in metal can be demonstrated in Fig. 10 and discussed as follows:

In Fig. 10a the dashed line is the solution of Eq. (1) for a fixed metal/oxide interface at $x = 0$ using the best-fit value for $D$ of the COMSOL calculation. A simple translation of this solution to 16 μm, the distance which the metal/oxide interface has advanced within 1320 days, yields the red solid line. The results of the COMSOL calculation which correctly account for a metal/oxide interface moving linearly with time, is illustrated by the blue solid line. As can be seen the shape of the COMSOL calculation is much steeper and the profile extends much less farther into the metal domain, in agreement with the experimental results. For the analytical solution, subsequently one has to reduce the COMSOL best-fit value for the diffusion coefficient by a factor of 30 from $D = 60 \times 10^{-21}\ m^2\ s^{-1}$ down to $D = 2 \times 10^{-21}\ m^2\ s^{-1}$ in order to achieve a "comparable fit" for the oxygen distribution in the metal (as presented in Fig. 10b). However, there remains a pronounced discrepancy in the asymptotic part which is due to the moving boundary accounted for correctly in the COMSOL calculation. Hence, the moving metal/oxide interface has an important and non-negligible effect on the modelling, its results and the conclusions drawn.

As mentioned before, the diffusion in the oxide being a non uniform process, it is not possible to perform a modelling to calculate the diffusion coefficients in the oxide. The assumption that the time for diffusion has been equivalent to the time of stay in the reactor does not seem realistic, as the calculations using the $D * t$ product obtained from the Origin 7 modelling yield diffusion

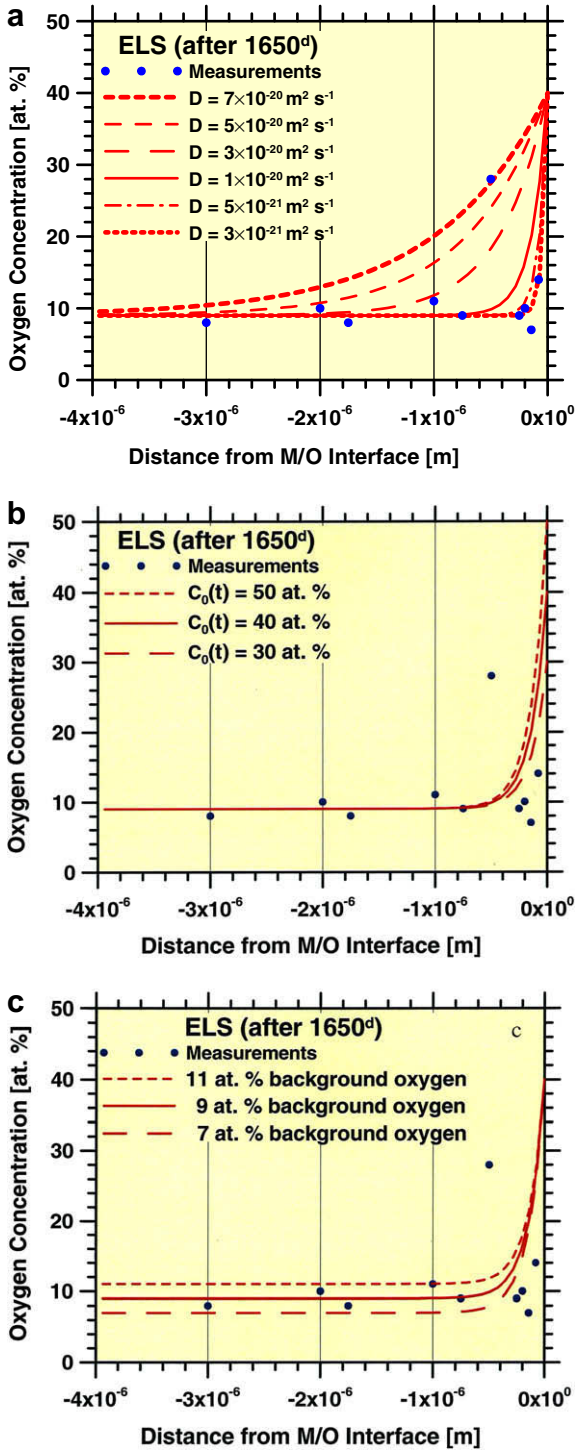


**Fig. 9.** Sensitivity analysis in the frame of the moving boundary model (COMSOL) for ELS material. (a) Variation of the value for the diffusion coefficient (Data for $C_1 = 40$ at.% and $C_0 = 9$ at.% remained fixed.); (b) the effect of modifying the oxygen concentration at the metal–oxide interface i.e. $C_1$; (c) the effect of modifying the oxygen concentration in the bulk metal i.e. $C_0$.

coefficients with a factor of $10^6$ smaller than the values reported in the literature. We assume however that the diffusion coefficient of oxygen in the oxide should also be different for the three alloys.

Assuming a linear oxidation rate using a moving boundary, the COMSOL calculations for the diffusion coefficient in the metal would be influenced by the diffusion coefficient of oxygen in the oxide layer. From the present observations, it is concluded,

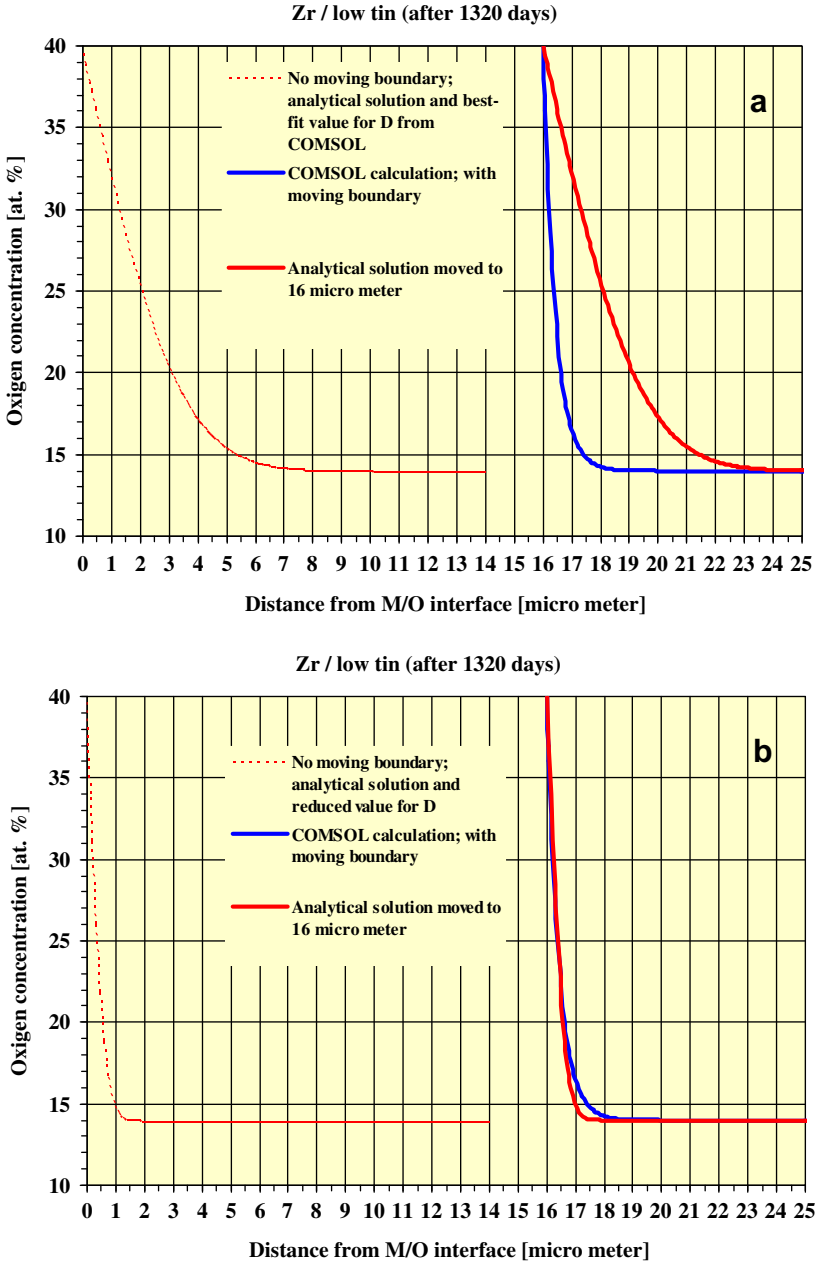


**Fig. 10.** Comparison of the results based on Eq. (1) and those of a COMSOL calculation with a moving boundary for the case of low-tin Zry-4. (a) Results of Eq. (1) and of a moving boundary calculation using COMSOL and (b) results of the Eq. (1) using a reduced value for $D$ (for further details see text).

that for the long oxidation times and linear oxidation rates as it is the case in the present materials, this influence is not very large. The reason for this is that the moving boundary calculation takes into account a certain time-dependent flux of oxygen to the metal–oxide interface. If the supply to this interface would go through a fixed thickness of oxide (which is accounted for in the discussion of barrier layer and is moving with the boundary), the overall flux will be further reduced, and hence the supply of oxygen influences the concentration $C_1$ at the metal/oxide interface. However, the sensitivity analysis has demonstrated that the calculations have a small sensitivity to the value for oxygen concentration at the metal–oxide interface.

The present findings are opposing the assumptions made in [7,8] that faster corroding alloys should lead to lower oxygen concentrations in the α-Zr(O) phase. On the other hand, the same references also mention the scarcity of, and difficulties to obtain such oxygen profiles. We argue that the higher oxygen concentrations in the metal phase for the Zircaloy-4 sample (s) mean a higher partial oxygen pressure in the α-Zr(O) at the interface. As the partial oxygen pressure thermodynamically limits the oxidation reaction (according to the Ellingham diagram in [7] $10^{-80}$ atm are needed at $T = 350\,^{\circ}C$ for the reaction to be allowed) this faster reached condition in the Zircaloy-4 case could explain the higher corrosion rate compared to the Zr/Nb and ELS alloys. Our results lead to the conclusion that the diffusion coefficient of oxygen in the metal is at least partly responsible for the difference in oxidation rate of the different alloys.

## 5. Summary

Analytical TEM on FIB-prepared corroded fuel cladding samples allowed to measure oxygen profiles close to and at both sides of the waterside metal/oxide interface. At this interface evidences clarifying the mechanism of ongoing corrosion process can be expected. The profiles from real, power plant exposed cladding alloy variants have proven that the concept of an innermost impervious oxide layer with diffusion-controlled oxygen access to the underlying metal is valid, although this barrier might be very thin. In the case of the fastest corroding Zry-4 sample(s) the diffusion-controlled layer was limited to approximately 200 nm only. The corresponding oxygen profiles in the underlying base metal are quite unique as such data otherwise are only available from corrosion experiments at much higher temperatures, linked e.g. to fuel cladding LOCA accident scenarios. The results qualitatively indicate a higher oxygen concentration at the interface and a broader diffusion profile in the case of the fastest corroding Zry-4 sample(s), revealing, at the same time, the thinnest oxygen diffusion zone in the oxide. Applying a diffusion model with a moving M/O boundary results in calculated diffusion coefficients in the metal in the range of $6 \times 10^{-20}\,m^2\,s^{-1}$ for Zry-4 and $1 \times 10^{-20}$ and $0.8 \times 10^{-20}\,m^2\,s^{-1}$ for the more corrosion-resistant cladding variants ELS and Zr/Nb, respectively. In the light of Ellingham diagrams, indicating the lower bound for the oxygen partial pressure necessary to convert the thermodynamically more stable α-Zr(O) into $ZrO_2$, the higher oxygen concentration and broader oxygen profile in Zry-4 suggest a combined thermodynamic and kinetic corrosion rate control.

## Acknowledgements

The authors wish to thank Gösgen power plant (KKG) for their supply of materials, Swissnuclear for their financial support for this work and Mr. J. Tharian from Swiss Federal Institute for Materials Testing and Research (EMPA) for the FIB sample preparation. The authors would also like to acknowledge the contribution and improvement to this paper by an anonymous reviewer.

## Appendix

The initial mesh (a) used for the COMSOL calculation at the $t = 0$ and the same mesh strongly zoomed (b).

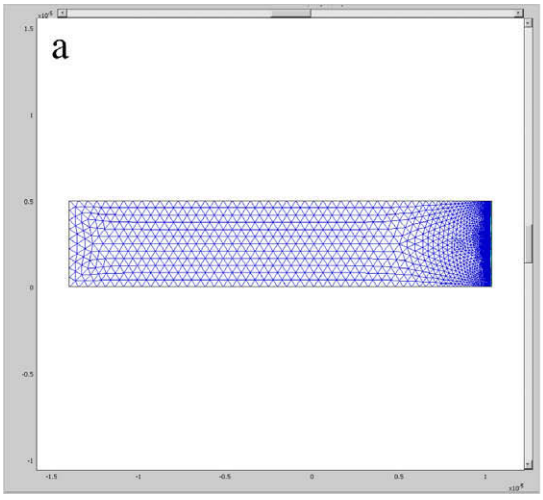


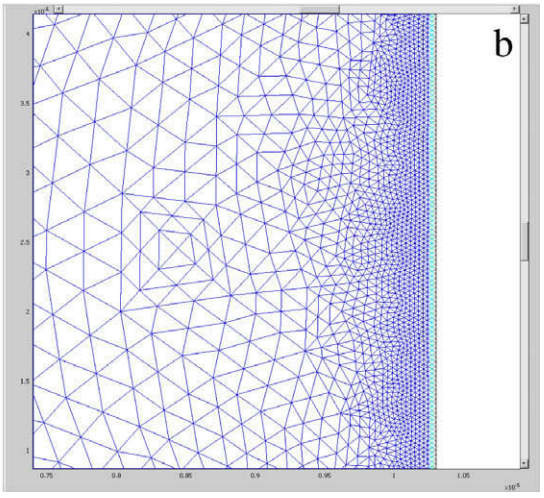


## References

[1] S. Abolhassani et al., Journal of ASTM International 2 (6) (2005).
[2] W.E. Wang, D.R. Olander, Journal of Nuclear Materials 201 (1993) 231–237.
[3] A. Grandjean, Y. Serruys, Journal of Nuclear Materials 273 (1) (1999) 111–115.
[4] J.P. West, et al., Challenges for the Nuclear Fuel – A Utility Perspective in Light-Water-Reactor-Fuel-Performance, Park City Utah, ANS, Illinois, USA, 2000.
[5] G. Ledergerber et al., Journal of Nuclear Science and Technology 43 (9) (2006) 1006–1014.
[6] J.D.M. Arborelius et al., Journal of ASTM International 2 (10) (2005).
[7] IAEA (Ed.), Waterside Corrosion of Zirconium Alloys in Nuclear Power Plants. TECDOC 996, IAEA, Vienna, 1998.
[8] IAEA (Ed.), Corrosion of Zirconium Alloys in Nuclear Power Plants. IAEATECDOC-684, IAEA, Vienna, 1993.
[9] S. Abolhassani, P. Gasser, Journal of Microscopy-Oxford 223 (2006) 73–82.
[10] P.L.G. Bossis, P. Barberis, X. Iltis, F. Lefebvre, Zirconium in the nuclear industry, Twelfth International Symposium ASTM STP 1354 (2000) 918–945.
[11] M.G. Glavicic, J.A. Szpunar, Y.P. Lin, Journal of Nuclear Materials 245 (1997) 5.
[12] Y.P. Lin, O.T. Woo, Journal of Nuclear Materials 277 (2000) 11–27.
[13] D. Khatamian, S.D. Lalonde, Journal of Nuclear Materials 245 (1) (1997) 10–16.
[14] C. Toffolon et al., Journal De Physique IV 11 (Pr1) (2001) 99–108.
[15] H.G. Kim, Y.H. Jeong, T.H. Kim, Journal of Nuclear Materials 326 (2-3) (2004) 125–131.
[16] B. Cox, Journal of Nuclear Materials 25 (3) (1968) 310–321.
[17] A.P. Zhilyaev, J.A. Szpunar, Journal of Nuclear Materials 264 (3) (1999) 327–332.
[18] A. Yilmazbayhan et al., Journal of Nuclear Materials 324 (1) (2004) 6–22.
[19] J.P. Pemsler, Journal of Nuclear Materials 7 (1) (1962) 16–25.
[20] B.J. Flinn, C.S. Zhang, P.R. Norton, Physical Review B 47 (24) (1993) 16499–16505.
[21] B.P.J.P. Cox, Journal of Nuclear Materials 28 (1968) 73–78.
[22] G.R. Wallwork, W.W. Smeltzer, C.J. Rosa, Acta Metallurgica 12 (4) (1964) 409–415.
[23] S. Nanikawa, Y. Etoh, Journal of Nuclear Science and Technology 38 (6) (2001) 420–428.
[24] P. Kofstad, High Temperature Corrosion, Elsevier Applied Science, London, 1988.
[25] G. Beranger, P. Lacombe, Journal of Nuclear Materials 16 (2) (1965) 190–207.
[26] J. Debuigne, Contribution à l0étude de l0oxydation du zirconium et de la diffusion de l0oxygène dans l0oxyde et dans le metal, PhD thesis, CNRS A.O.21.03, INSA Rennes, 031772L, 1966.
[27] G.A. Eloff, C.J. Greyling, P.E. Viljoen, Journal of Nuclear Materials 199 (3) (1993) 285–288.
[28] Origin7, OriginLab Corporation, Northampton, MA 01060, USA. <http://www.originlab.com>.
[29] B. Hutchinson et al., Journal of ASTM International 4 (10) (2007).
[30] D. Hudson, A. Cerezo, G.D.W. Smith, Ultramicroscopy 109 (2009) 667–671.
[31] COMSOL/Multiphysics, COMSOL AB, Stockholm, Sweden. <http://www.comsol.com>.